ACS APPLIED MATERIALS & INTERFACES

Research Article

www.acsami.org

Influence of Chemical Microstructure of Single-Ion Polymeric Electrolyte Membranes on Performance of Lithium-Ion Batteries

Yunfeng Zhang,[‡,†] Rupesh Rohan,[‡] Weiwei Cai,[‡] Guodong Xu,[‡] Yubao Sun,[*,†] An Lin,[§] and Hansong Cheng[*,‡,†]

[†]Sustainable Energy Laboratory, Faculty of Material Science and Chemistry, University of Geosciences (Wuhan), 388 Lumo RD, Wuhan 430074, China

[‡]Department of Chemistry, National University of Singapore, 3 Science Drive 3, 117543 Singapore

[§]College of Resource and Environmental Science, Wuhan University, Wuhan 430072, China

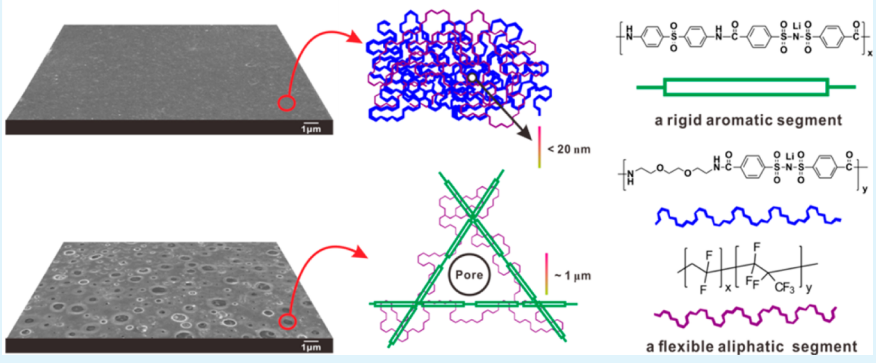

ABSTRACT: A novel protocol to generate and control porosity in polymeric structures is presented for fabrication of single ion polymer electrolyte (SIPE) membranes for lithium ion batteries. A series of SIPEs with varying ratios of aliphatic and aromatic segments was successfully synthesized and subsequently blended with PVDF-HFP to fabricate membranes of various sizes of pores. The membranes were characterized using techniques including SEM, solvent uptake capacity measurement and ionic conductivity. We demonstrate that appropriate membrane porosity enhances ionic conductivity, reduces interfacial resistance between electrodes and electrolyte and ultimately boosts performance of Li-ion batteries. The implication of the structure–performance relationship for battery design is discussed.

KEYWORDS: *lithium-ion batteries, porous architecture, energy storage, polymer electrolyte, battery performance*

1. INTRODUCTION

There has been an increasing demand for safe, low-cost, and efficient energy storage technologies with lithium-ion batteries.[1−5] A battery electrolyte with high ionic conductivity and thermal and electrochemical stability is one of the most critical components of battery devices.[6] In the past few years, several solid and gel polymer electrolytes based on the concept of single-ion conduction have been developed.[7−9] Unlike dual-ion electrolytes comprised of small lithium salts either dissolved in selected organic solvents or blended in polymer matrices with or without solvents,[10−12] concentration polarization effect upon charge/discharge is minimized in single-ion electrolytes. Here, the anions, bis(sulphonyl) imide, $(SO_2)_2N^-$ (BSI), are anchored on polymer chains and thus immobile; the negative charges of the bis(sulphonyl) imide groups are delocalized in the proximity of the active sites driven by the neighboring electron-withdrawing groups of sulphonyl, which enables lithium ions to be weakly attached to the polymer through an electrostatic interaction with high mobility.[8,13,14] Several studies have demonstrated that the ion transference number of single-ion polymer electrolytes (SIPEs) is close to unity,[13−15] whereas the value for most dual-ion electrolytes is only a small fraction.[16,17] According to the Nernst–Planck equation,[18] ion conduction is largely dictated by both ion diffusivity, determined by lithium salt concentration and solvent viscosity, and ion transference number, driven by an electrochemical field.[19] Therefore, SIPEs are highly advantageous, compared to conventional dual-ion electrolytes, if ion diffusivity in these materials can also be enhanced. This can be realized by allowing selected organic solvents to flow into the polymer matrix with appropriate pores to facilitate ion diffusion, as demonstrated in our previous work, where ionic conductivity of the functionalized meso/macroporous single ion conducting electrolyte membrane was found to be on the order of 1×10^{-3} S cm^{-1} at room temperature.[20] Aside from the high ionic conductivity, SIPE materials have also been found to be thermally and electrochemically more stable than conventional liquid electrolytes in a broad temperature range[20,21] and thus are well-suited

Received: May 21, 2014
Accepted: September 16, 2014
Published: September 16, 2014

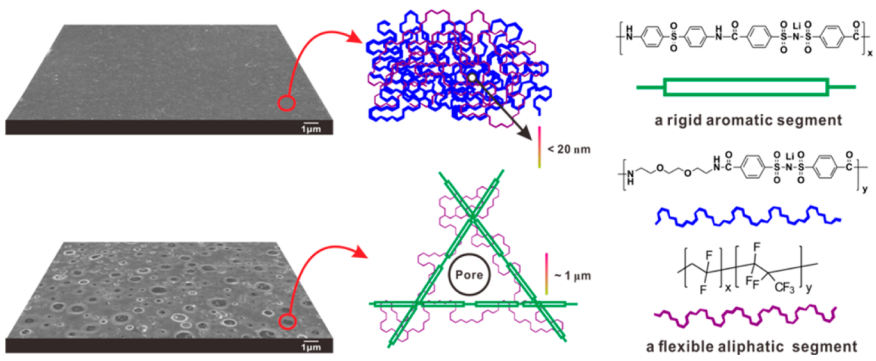

Figure 1. Schematic illustration of structure design for porosity control of SIPE membranes.

Scheme 1. Procedure for the Synthesis of the SIPEs

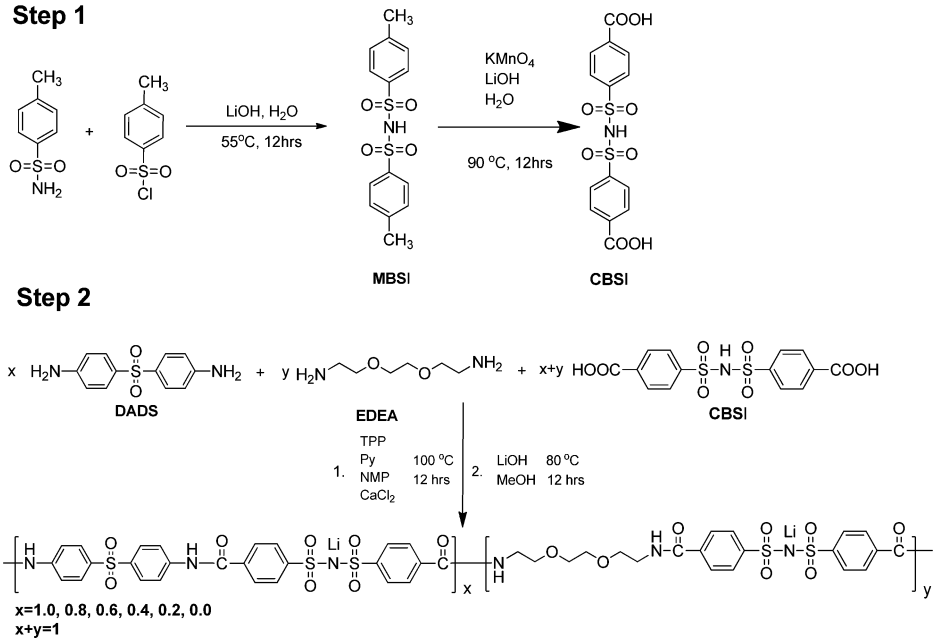

for safe operation of battery devices for a wide variety of applications. The high thermal stability of SIPEs arises mainly from the selected polymer backbones.[22] The electrochemical superiority of SIPEs over conventional liquid electrolytes results from the fact that in SIPEs, anions are tethered to polymer chains and can be oxidized only at the interface[22] and the substantially less concentration polarization inherent to this class of materials.[14,17,23]

In general, ion conduction in a SIPE membrane comprised of a SIPE complex and a binder, which provides the required mechanical and thermal strength and flexibility to the membrane, must possess proper migration channels to allow Li ions to move along the polymer walls to minimize polarization arising from a large charge separation. Therefore, the ionic conductivity is also strongly influenced by the morphology, the size and type of pores of the membrane. Two fundamentally important issues thus arise:

Are the morphology and pore distribution of a SIPE membrane controllable?

How do the electrochemical properties vary with SIPE composition and microstructure?

Despite intense recent development of SIPE materials, these issues have not been well-understood to date. In this paper, we report our attempt to address these important issues by testing electrochemical properties and battery performance with a series of SIPE membranes with controlled morphology and pore channels. The main idea is to design polymer electrolytes with appropriate rigidity and flexibility to control the morphology, the type and size of pores and ion conduction channels for optimizing electrochemical properties of battery devices. The relationship between the microstructure of SIPE membranes and battery performance is thus revealed. The study sheds a light for design of safe, high performance of Li-ion batteries using SIPE membranes.

It has been a consensus that an aromatic segment is considered rigid and an aliphatic segment is deemed flexible in a polymer. The contrasting nature of the two moieties can be utilized to produce pores of a variety of types and sizes upon blending with a binder. If the binder is an aliphatic long chain polymer,e former and poor compatibility with the latter. Mechanistically, the aliphatic polymer en then upon blending with an aliphatic polymer and an aromatic polymer separately, the morphologies of the blends would appear as shown in Figure 1 with strong compatibility with thtangles with the binder smoothly with nanoscale phase separation while the aromatic polymer produces pores upon blending with the

Table 1. Designation of SIPEs Based on the Proportion of DADS and EDEA

DADS:EDEA	1:0	0.8:0.2	0.6:0.4	0.4:0.6	0.2:0.8	0:1
designation	DE10	DE82	DE64	DE46	DE28	DE01

Table 2. Elemental Analysis of the SIPEs

designation	C (wt %) (theoretical)	H (wt %) (theoretical)	N (wt %) (theoretical)	S (wt %) (theoretical)	Li (wt %) (theoretical)
DE 10	46.46 (51.74)	3.22 (3.01)	6. 82 (6.96)	15.66 (15.94)	1. 09 (1.15)
DE 82	45.55 (51.04)	3.49 (3.25)	6.36 (7.20)	13.59 (15.39)	1.10 (1.19)
DE 64	45.52 (50.30)	3.66 (3.51)	6.86 (7.46)	12.98 (14.79)	1.22 (1.23)
DE 46	45.22 (49.50)	4.05 (3.78)	7.20 (7.73)	12.50 (14.16)	1.22 (1.28)
DE 28	44.64 (48.64)	4.28 (4.08)	7.28 (8.03)	12.06 (13.48)	1.19 (1.33)
DE 01	42.34 (47.71)	4.40 (4.40)	7.36 (8.35)	10.86 (12.74)	1.24 (1.38)

aliphatic binder due to its molecular rigidity. As a consequence, the aliphatic blend displays virtually nanoscale phase separation, whereas the aromatic blend exhibits micropores with types and sizes depending largely on the microstructures of the SIPE materials as well as the amount of binders. The ratio of aromatic and aliphatic segments contained in a polymer thus becomes a decisive factor for control of pore size and type and pore distribution in the membrane.[24] Consequently, the porosity of the polymer can be altered by tuning the ratio of aromatic/aliphatic segments, providing great flexibility for design of novel SIPE membranes to achieve high performance of battery cells. In the present study, we selected PVDF-HFP as the binder to take advantage of its compatibility with the aliphatic segments and its incompatibility with the aromatic segments of the polymer synthesized to gain control of porosity of the SIPE membranes.

2. EXPERIMENTAL SECTION

2.1. Materials. 2,2′-(Ethylenedioxy) bis(ethylamine) (EDEA), 4,4′-diaminodiphenylsulfone (DADS), *p*-toluenesulfonamide, *p*-toluenesulfonyl chloride, $KMnO_4$, PVDF-HFP, LiFePO4, triphenylphosphine oxide (TPP), dimethylformamide (DMF), methanol, and acetylene black were purchased from Sigma-Aldrich. 2,2′-(ethylenedioxy) bis(ethylamine) (EDEA), triphenylphosphine oxide (TPP), dimethylformamide (DMF) and methanol were used as received without further purification. DADS was dried at 100 °C for 24 h. Pyridine was dried with KOH and distilled. *N*-Methyl-2-pyrrolidone (NMP) was distilled from P_2O_5 and calcium chloride ($CaCl_2$) was dried under vacuum at 180 °C for 24 h before use.

2.2. Synthesis of Bis(4-carboxyl benzene sulphonyl) Imide (CBSI). *2.2.1. Synthesis of bis(4-methy benzene sulphonyl) imide (MBSI).* The synthesis of the MBSI is shown in Scheme 1 (Step 1). A homogeneous solution was prepared by dissolving *p*-toluenesulfonamide (17.122 g, 100 mmol) and NaOH (4.225 g, 105 mmol) into 150 mL of deionized water at 95 °C. Subsequently, *p*-toluenesulfonyl chloride (19.074 g, 100 mmol) was slowly added into the solution in 2 h, and the reaction was then kept at 95 °C for another 12 h. After adjusting the pH of the mixture to 7 by using diluted HCl, the reaction was kept overnight. A sufficient amount of HCl was added to adjust the pH of the solution to 1, yielding a white precipitate. The product was collected via filtration and then dried under vacuum overnight at 120 °C. The final product (20.665 g) was obtained upon recrystallization from the deionized water. The yield was 63.5%. ^{1}HNMR (DMSO-d_6): 7.57 (d, 2H), 7.25 (d, 2H), and 2.35 (s, 3H).

2.2.2. Synthesis of Bis(4-carboxyl benzene sulphonyl) Imide (CBSI). Synthesis of the bis(4-carboxyl benzene sulphonyl) imide (CBSI) was conducted in a similar procedure to what was reported in our earlier work (Scheme 1 (Step 1)).[25] 4, 4′-dicarboxyldiphenylsulfonimide monomer was obtained by oxidizing the methyl group of MBSI into a carboxyl group. 4, 4′-dimethyldiphenylsulfonimide (20.665 g, 63.51 mmol) and LiOH·H_2O (2.690 g, 63.51 mmol) were then dissolved completely into deionized water (300 mL) at 95 °C. $KMnO_4$ (20.068 g, 127.0 mmol) was slowly added to the solution in 2 h. Subsequently, the reaction mixture was stirred at 95 °C overnight. Upon removal of MnO_2 and the unreacted $KMnO_4$ by filtration, the filtrate was acidified with concentrated HCl. After repeating the acidification process 5 times, the final product was collected with a yield of 76.1%. ^{1}HNMR (DMSO-d6): 7.93 (d, 2H), 7.76 (d, 2H). Elemental analysis result: C, 39.8 wt % (theoretical 43.63 wt %); H, 2.22 wt % (theoretical 2.88 wt %); N, 3.23 wt % (theoretical 3.63 wt %); and S, 15.25 wt % (theoretical 16.64 wt %).

2.2.3. Synthesis of the SIPEs. The synthesis route of the SIPEs is shown in Scheme 1. The designation of the SIPEs based on the proportion of DADS and EDEA is listed in Table 1. Six sets of mixtures, each containing CBSI 1.0 mmol (0.385 g), TPP 2 mmol (0.52 mL), NMP 2.0 mL, pyridine 1.5 mL, and $CaCl_2$ 0.28g (~8 wt %), were weighed and transferred into two 100 mL round-bottom flasks. Subsequently, 2,2′-(ethylenedioxy) bis(ethylamine) (EDEA) and 4,4′-diaminodiphenylsulfone (DADS), were added to the solutions by varying their proportions to form the designated SIPEs. All mixtures were stirred and heated at 100 °C under argon atmosphere for 12 h. Upon completion of the reactions, the solutions were cooled to 70 °C and transferred into an excess of cold methanol and placed in an ice-bath under stirring. The suspensions were then filtered, and the precipitates were washed with methanol and water continuously followed by drying at 140 °C under vacuum for 24 h. The yields were above 95% in all cases. Lithiation of the products were performed by reacting the compounds with LiOH in the stoichiometric ratio for overnight in a methanol medium. The process was repeated three times to ensure complete lithiation. The final products were washed by methanol and then dried at 120 °C for 24 h. Finally, the products were kept in an argon-filled glovebox for further characterizations. The elemental analysis (Table 2) and gel permeation chromatography (GPC) (Table 3) demonstrate the expected materials were obtained.

Table 3. Molecular Weights of the SIPEs

designation	M_n ($\times 10^4$)	M_w ($\times 10^4$)	M_w/M_n
DE 10	4.45	8.34	1.87
DE 82	4.33	8.62	1.99
DE 64	7.41	11.86	1.60
DE 46	8.99	13.31	1.48
DE 28	10.35	14.59	1.41
DE 01	10.82	15.47	1.43

2.2.4. Preparation of the SIPE Membranes. To fabricate PVDF-HFP/SIPE membranes, the equivalent mass of PVDF-HFP and the target materials were dissolved in DMF and the solutions were cast onto glass plates and kept at 80 °C overnight, and then dried at 80 °C under vacuum for 48 h. The photographs of the selected SIPE blend polymer membranes are shown in Figure 2. Finally, the prepared SIPE blend polymer membranes were transferred into an argon-filled glovebox and soaked in an EC/PC (v:v, 1:1) solvent for further characterizations.

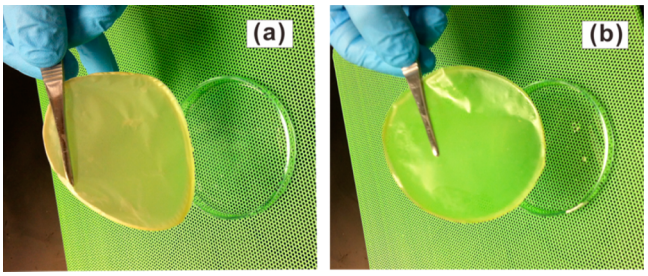

Figure 2. Photographs of (a) the DE10-based membrane and (b) the DE01-based membrane.

2.2.5. Preparation of the $LiFePO_4$ Cathode. To analyze the battery performance, we used a multichannel battery testing instrument Arbin BT-2000 for discharge capacity measurement of coin cells assembled with the synthesized polymeric electrolyte membranes. A composite cathode was prepared by casting a well-stirred solution of $LiFePO_4$ (75 wt %), PVDF (10 wt %), acetylene black (10 wt %), and LiCBSI (5 wt %) as a supporting electrolyte in a NMP solvent onto an aluminum foil. The resulting electrode was initially dried at 60 °C and further dried at 60 °C in a vacuum oven for 12 h. The dried cathode was then cut into a circular shape used in coin cells. The assembling of the standard coin cells (CR2025) was done inside a glovebox.

2.3. Characterization. GPC measurements were performed using a Waters GPC system, equipped with a Waters 1515 isocratic HPLC pump, a Waters 717 plus Autosampler injector, a Waters 2414 refractive index detector, and a Agilent PL gel 5 μm mixed-D column (P/N: 79911GP-MXD), using N,N′-dimethylformamide as the eluent at 50 °C and at a flow rate of 1.0 mL min^{-1}. Tensile tests of the membranes were performed using an Instron universal materials testing system (model 5544) with a 10 N load cell in a constant relative humidity (50%) room at 25 °C. Rectangular-shaped samples were cut from the membranes (5 mm wide with a gauge length of 10 mm). The thickness of the samples was measured with a digital micrometer having a precision of 1 μm. A cross-head speed of 10 mm/min was used. The calibration curve was generated using polyethylene glycol molecular weight standards. All infrared spectra were taken with a Bio-Rad Excalibur FTIR spectrometer in the 400−4000 cm^{-1} frequency range. ^{1}H NMR spectra were recorded on a Bruker AMX (500) spectrometer at 300 MHz. Dimethyl sulfoxide-d6 was used as solvents for NMR test. The morphologies of polymer electrolytes were probed using the scanning electron microscopy (SEM) with QUANTA 200 FEG. Samples were prepared by platinum sputtering under 5×10^{-2} mbar at room temperature (20s, 30 mA) with a Baltec SCD050 apparatus. The thermal degradation study was performed under inert atmosphere of N_2 (flow rate: 60 cm^3 min^{-1}), at the 10 °C min^{-1} heating rate in the Thermo Gravimetric Analyzer (model TGA Q 50) of TA, Inst., USA. The thermal stability test was conducted from room temperature to 600 °C.

The ion conductivity of the polymer electrolytes was measured by electrochemical impedance spectroscopy (EIS) using the Zahner potentioastat-galvanostat electrochemical workstation model, PGSTAT, with the EIS module over a frequency range of 4×10^6 to 1 Hz and an oscillating voltage of 5 mV. A stainless steel cylindrical device of 1.5 cm diameter was used for conductivity measurement. The fitting of the raw data was done by using the simulated impedance measurement (SIM) software. The electrochemical stability test (cyclic voltammetry) was conducted in the same stainless steel device using the CHi instrument in the voltage range of 1.5−7 V at a scan rate of 2 mV S^{-1}. A circular thin sheet of lithium metal along with the electrolyte membrane was placed inside the cavity of the device and sealed in a glovebox under argon atmosphere. The lithium-ion transference number, t^+, defined by $t^+ = I_s(\Delta V - I_oR_o)/I_o(\Delta V - I_sR_s)$, ΔV is the potential applied across the cell, I_o and I_s are the initial and steady-state currents and R_o and R_s are the initial and steady-state resistances of the passivation layers on the Li electrode,[26] was measured with the Li|SIPE membranelLi battery cell, in which an electrolyte membrane soaked in a EC/PC solution was mounted between the two nonblocking lithium metal electrodes.[27,28]

3. RESULTS AND DISCUSSION

3.1. Characterization of the SIPEs. The FTIR spectra of the SIPEs are shown in Figure 3. The characteristic bands

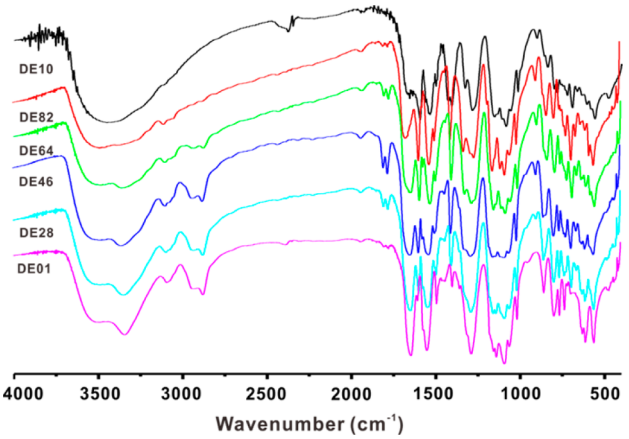

Figure 3. FTIR spectra of the SIPEs.

around 3400 cm^{-1} (N−H) represent the N−H stretch of the sulfonimide group in the copolymer side chains. The band near 1600−1500 cm^{-1} corresponds to the C═O stretch of the amide group. The absorption band in the range of 3000−3100 cm^{-1} is assigned to the C−H stretching frequency of benzene. The intensity of the characteristic band near 2800−3000 cm^{-1}, which corresponding to the C−H stretching of the alkyl chains in the SIPEs, increases as the aliphatic group content increases.

The chemical structures of the SIPEs are supported by the ^{1}HNMR spectra. Figure 4 shows the ^{1}HNMR spectra of the SIPE series. The signals of the hydrogen (H_a and H_c) on the aliphatic chains can be easily identified. The signals of the hydrogen (H_d and H_e) are assigned to the CBSI precursor and the signals of the hydrogen (H_h and H_g) are attributed to the DADS precursor. The intensity of the H_a and H_c signals rises proportionally with the amount of EDEA precursor. In

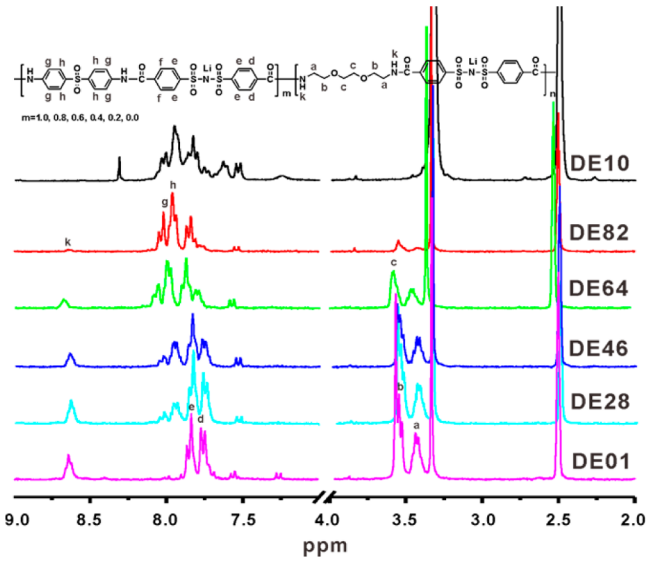

Figure 4. ^{1}HNMR spectra of the SIPEs.

dx.doi.org/10.1021/am503152m | ACS Appl. Mater. Interfaces 2014, 6, 17534−17542

contrast, the intensity of the H_a and H_c signals decreases proportionally with the amount of EDEA precursor. The results confirm a successful synthesis of the aromatic−aliphatic hybrid backbone structures of SIPEs.

3.2. Morphologies of the SIPE Membranes. The SEM images of the membranes, shown in Figure 5, validate the proposed concept explicitly. The DE10 membrane shows a highly porous structure (Figure 5a) with a uniform distribution of pores throughout the membrane while the cross-section image (Figure 5a′) confirms the presence of pores inside the membrane. The magnified images of Figure 5a are shown in Figure 6. As shown in Figure 6, the porous structure is clearly observed from the "white plots" of the membranes. The DE82 membrane displays (Figure 5b) relatively a fewer number of pores than the previous membrane and the appearance of the pores becomes blind rather than open. The image of its cross-section (Figure 5b′) indicates the presence of some stretched pores formed due to the fractured layer of the membrane. In the DE64 membrane, the size and the number of the blind pores decrease further (Figure 5c) and the cross-section image exhibits a few blind and irregular pores. The other membranes (DE46, DE28, and DE01) show very small blind pores on membrane surfaces (Figure 5d−f) and virtually no pores are observed in their cross section images (Figure 5d′−f′). Indeed, the SEM images confirm that the presence of rigid aromatic content in the membrane regulates its porosity. The aromatic segments disrupt the smoothness of the membrane and facilitate formation of pores. As the aromatic component in the polymer increases, the porosity becomes increasingly visible in both surfaces and cross-sections of the membranes. We note that there appear more pores in d and e than in a and b in Figure 5. However, the sizbe of the pores in d and e is significantly smaller than the size of the pores in a and . Overall, the solvent capacity in a and b is still higher than in d and e, as will be made clear below.

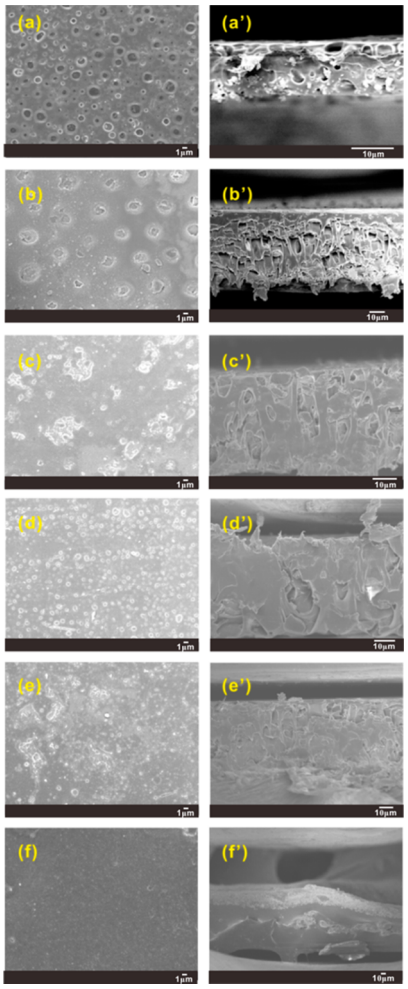

Figure 5. SEM images of the SIPE membranes. Surface: (a) DE10, (b) DE82, (c) DE64, (d) DE46, (e) DE28, and (f) DE01; cross-section: (a′) DE10, (b′) DE82, (c′) DE64, (d′) DE46, (e′) DE28, and (f′) DE01.

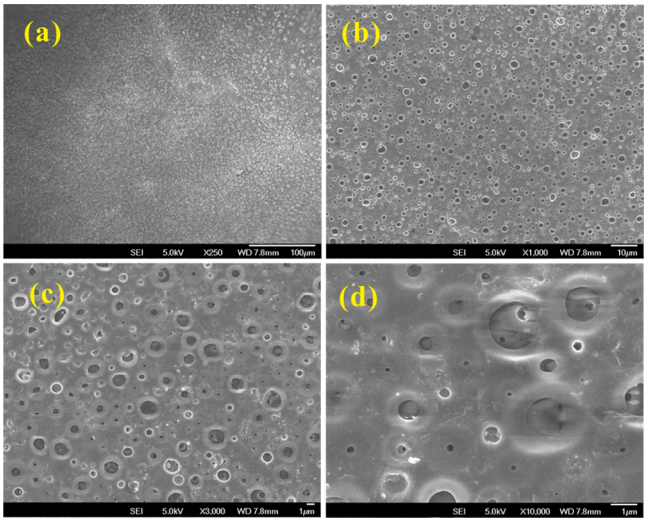

Figure 6. Surface SEM images of DE10 membrane with four different magnifications: (a) ×250, (b) ×1000, (c) ×3000, and (d) ×10000.

The porosity of the SIPE membranes was quantified by directly measuring solvent uptakes. All the membranes were immersed in the EC/PC (1:1v/v) solution for 3 days to measure their solvent uptake capacity shown in Figure 7. As anticipated, the capacity declines gradually from the DE10 based membrane to the DE01 based membrane. The results clearly substantiate the concept of SIPE membrane structural design and are consistent with the observation from the SEM images. In particular, the DE10 based membrane shows the highest solvent uptake of 211 wt %, confirming the formation of a highly porous structure. In contrast, the DE01 based

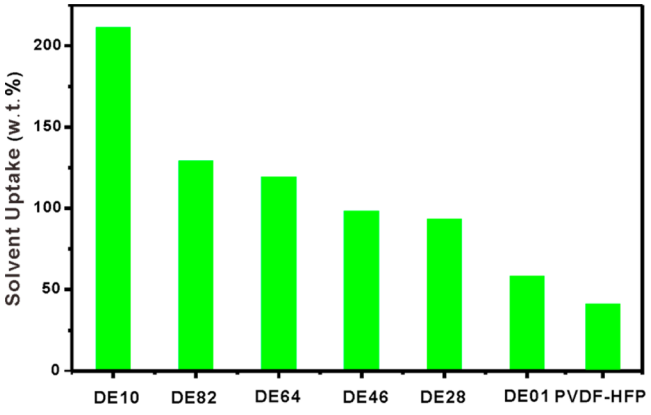

Figure 7. Solvent uptake of the SIPE membranes and the pure PVDF-HFP membrane.

dx.doi.org/10.1021/am503152m | ACS Appl. Mater. Interfaces 2014, 6, 17534−17542

membrane displays the lowest solvent uptake of 58 wt %. The solvent uptake of the pure PVDF-HFP was measured to be 41.9 wt %, which is attributed to the osmotic drive for the solvent to swell the PVDF-HFP matrix. Clearly, the results are consistent with the relative order of porosity shown in Figure 5.

3.3. Thermal Stability of the SIPEs. Figure 8 exhibits that the prepared SIPEs display excellent thermal stability up to 400

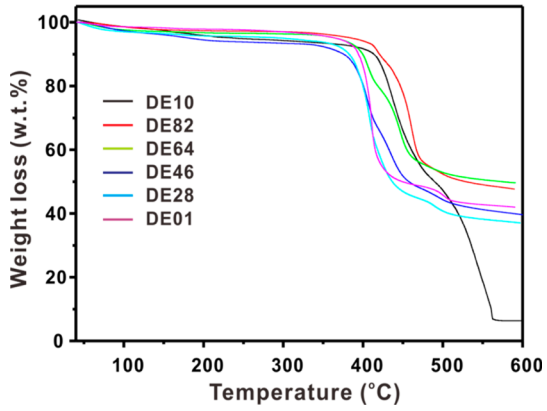

Figure 8. TGA spectra of the SIPEs.

°C. The small amounts of weight loss before 200 °C are attributed to desorption of moisture and NMP solvent. It concludes that all these materials surpass the thermal stability requirement for lithium-based batteries.

3.4. Electrochemical Stability of the SIPE Membranes. The electrochemical stability of the SIPEs was investigated using cyclic voltammetry (CV). Prior to the test, the prepared SIPE membranes were used to construct Li|SIPE membrane|stainless steels (SS) cells. The current−voltage response of the membranes tested with the Li|SIPE membrane|SS cells at room temperature is shown in Figure 9. Clearly, the fully aromatic DE10 based membrane shows high electrochemical stability up to 5.5 V and the other membranes are also electrochemically stable up to 4.7 V, providing a sufficiently wide electrochemical window to match up with cathode materials such as $LiCoO_2$, $LiMn_2O_4$, and $LiFePO_4$ for Li-ion battery applications.

3.5. Mechanical Property of the SIPE Membranes. Figure 10 shows the stress−strain curves of the blend membranes. The DE10 based membrane exhibits the best mechanical performance of 81.9 MPa, substantially higher than that of the DE01 based membrane of 37.7 MPa. The mechanical strength of the pure PVDF-HFP membrane was measured to be 23.1 MPa (Figure 10d), which is higher than the reported value of 10 MPa for PVDF-HFP ion gel.[29] As the aliphatic component increases from DE10 to DE01, the tensile strength decreases from 81.9 to 37.7 MPa, indicating that aromatic group gives rise to a superior tensile strength compared to aliphatic group in the aromatic/aliphatic polymers (Table 4). Indeed, aromatic groups have been found in a variety of polymeric materials to strengthen mechanical properties.[30] Our results indicate that it is the aromatic segments, not the porosity, that dictates the mechanical strengths of the SIPE membranes.

3.6. Ionic Conductivity and Lithium Ion Transference Number of the SIPE Membranes. The porosity of the membranes was found to profoundly affect the ionic conductivity and thus significantly influences the battery performance. The ionic conductivity of the membranes

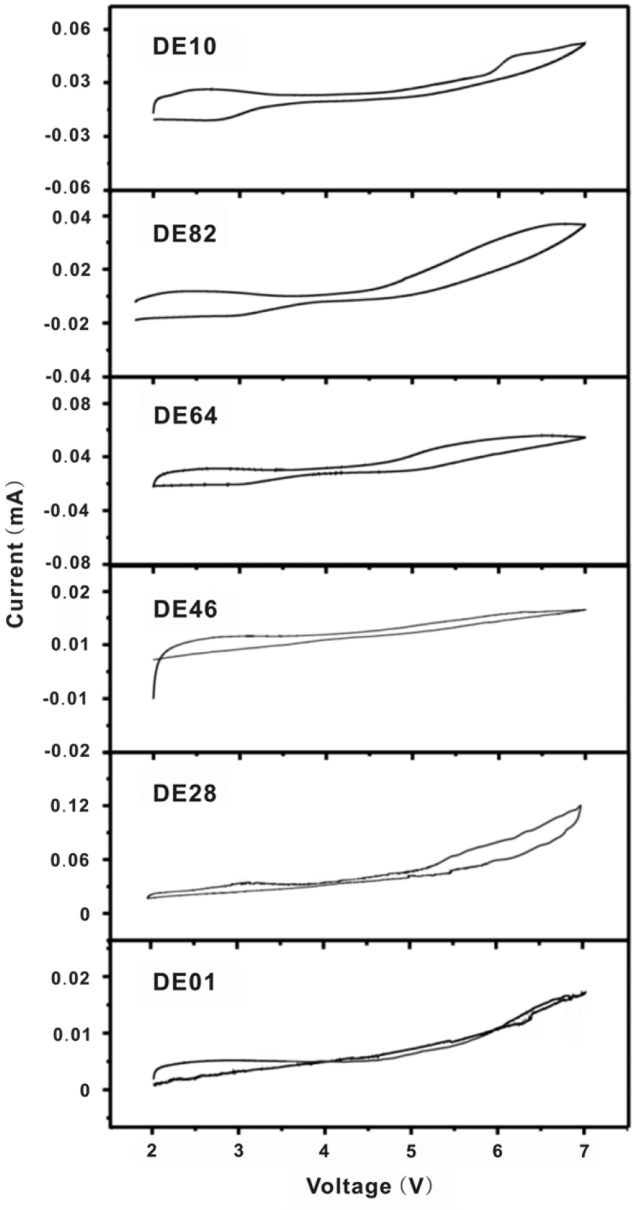

Figure 9. Electrochemical stabilities of the SIPEs.

measured in the temperature range from 80 °C to room temperature downward shown in Figure 11 clearly reveals the significance of membrane porosity. Essentially, the conductivity decreases monotonically with the reduction of structural porosity with the DE10 membrane displaying the highest conductivity and the DE01 membrane exhibiting the lowest conductivity in the entire temperature range. The room temperature conductivity of DE10 was found to be 4×10^{-4} S cm^{-1}, which is among the highest ionic conductivity displayed by SIPE membranes reported to date[9,31−34] and even comparable to the conductivity of the DE82 membrane at 80 °C. The high conductivity of the DE10 membrane is attributed to the high solvent uptake enabled by the high porosity and the smooth conduction channels of the membrane. As expected, the ionic conductivity of all membranes increases with temperature but, interestingly, not as steep as in typical gel polymer electrolytes because of the mechanical coupling between ion transport and polymer host mobility in accordance to the free volume law.[35−37]

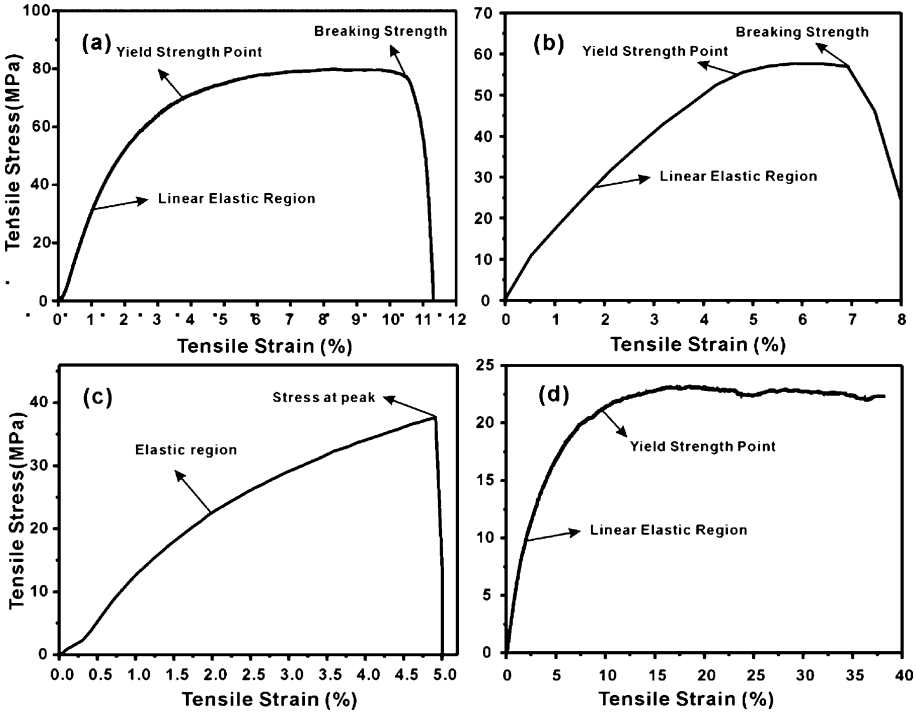

Figure 10. Stress–strain curves of the selected SIPE membranes. (a) The DE10 based membrane, (b) the DE64 based membrane, (c) the DE01 based membrane, and (d) the pure PVDF-HFP membrane.

Table 4. Mechanical Strengths of the SIPE Membranes

	DE10	DE82	DE64	DE46	DE28	DE01	PVDF-HFP
tensile stress (MPa)	81.9	65.7	57.7	49.8	40.9	37.7	23.1
elongation at break (%)	10.8	8.2	7.5	6.3	5.1	4.9	>38.2

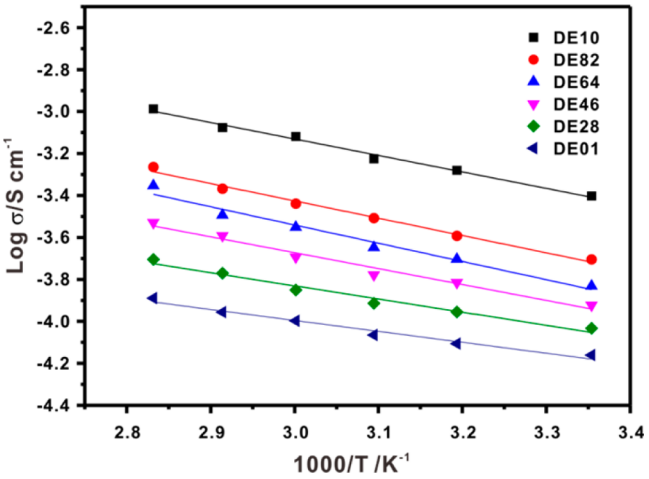

Figure 11. Temperature dependence of ionic conductivity of the SIPE membranes.

We note that the conductivity of the majority of electrolytes, including conventional dual-ion based liquid electrolytes of lithium salts and polymer electrolytes and single-ion polymer electrolytes, displays a linear behavior on an Arrhenius plot,[23,32,38] which suggests that the conductivity is largely dictated by an enthalpic barrier. An exception was recently found for a PEO based SIPE material at about 60 °C,[22,39] above which a nonlinear behavior was observed. The reason was attributed to the melting point of PEO at 60 °C, at which the phase transition gives rise to a large change of entropy and thus results in the observed nonlinear behavior. The SIPE membranes are thermally stable in the entire temperature range of the conductivity measurement, which explains the linear behavior of the Arrhenius plot as the enthalpic barrier dominates the conduction process.

A steady-state current method was used to measure lithium ion transference number on the Lilblend polymer membranelLi symmetric cell at room temperature. The results are summarized in Table 5. The measured lithium ion transference

Table 5. Measured Values for the Corresponding Calculated Values of Lithium-Ion Transference Numbers (t_{Li}^+)

electrolytes	I_0 (μA)	I_s(μA)	R_0 (Ω)	R_s (Ω)	$t_{Li}^+ = I_s(\Delta V - I_oR_o)/I_o(\Delta V - I_sR_s)$
DE10	1.41	1.27	27.30	27.99	0.90
DE 82	3.32	3.00	5.55	5.28	0.90
DE 64	4.34	4.02	17.127	17.353	0.92
DE 46	8.21	7.60	70.423	71.23	0.92
DE 28	1.23	1.12	6.77	5.64	0.91
DE 01	2.00	1.80	73.45	68.08	0.90

numbers of the blend SIPE membranes are approximately 0.90, suggesting that these membranes behave truly as single ion conductive electrolytes.

3.7. Electrochemical Performances of the SIPE Membranes. The EIS response of the battery cells assembled with a Li foil anode, a $LiFePO_4$ cathode and the SIPE membranes at room temperature in the Nyquist coordinates is depicted in Figure 12. The interfacial resistance of the cells increases from the DE10 cell to the DE01 cell, attributed to the porosity reduction. The solvent retained in the membrane pores effectively reduces the interfacial resistance between the

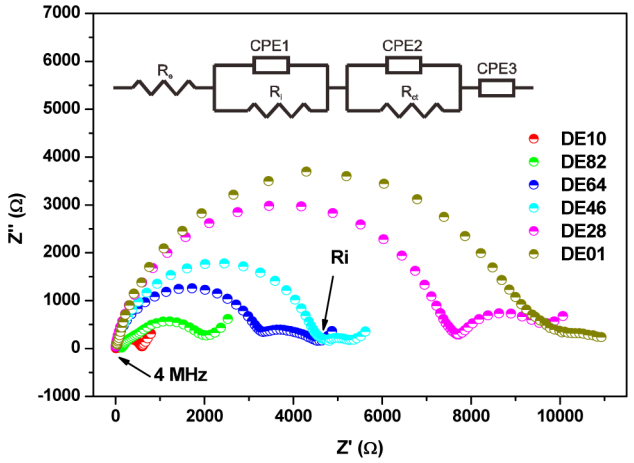

Figure 12. Nyquist plots with corresponding equivalent circuit shown in inset of the present SIPE membranes-based batteries at 25 °C.

electrodes and the electrolyte membrane and thus promotes facile transport of Li^+ ions in the battery cells.

All coin cells assembled using the six SIPE membranes are operative at an elevated temperature with performance varying significantly dependent on membrane porosity. The performance of the battery devices with selected SIPE membranes is shown in Figure 13. At 80 °C, the three selected cells, DE10, DE64, and DE01, display proper charge−discharge behavior (Figure 13a). The DE10 cell shows a discharge capacity in the range of 155−160 mAh g^{-1} at the discharge rate of 0.1 *C*, close to the theortical capacity of $LiFePO_4$ (170 mAh g^{-1}). The discharge capacity decreases modestly as the discharge rate increases. The DE64 cell displays a significant discharge capacity at 0.1 and 0.2 *C* and much lower discharge capacity of less than 5 $mAhg^{-1}$ was observed at higher discharge rates. The DE01 cell exhibits a substantially lower discharge capacity and approaches almost to zero at 0.5 and 1 *C*. At room temperature, the DE10 cell is the only one that performs well at various *C*-rates (Figure 13b). The results clearly indicate that battery performance deteriorates significantly as porosity of the membranes decreases and underscore the fact that the porous structure of SIPE membranes, along with the choice of materials for synthesis of SIPEs, is of critical importance for enhanced battery performance. Therefore, the tunability of porosity through structural design and membrane fabrication is essential for regulating battery operation. Judicious selection of precursors on the basis of their chemical microstructures provides the ultimate tunability for SIPE material design.

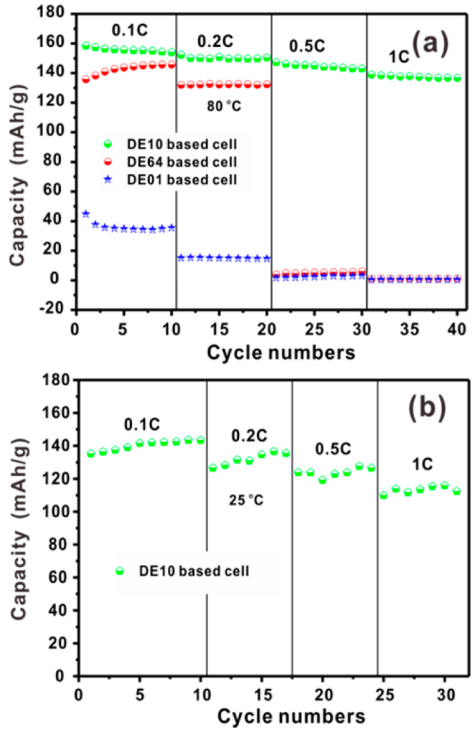

Figure 13. (a) Cycle-life of the selected SIPEMs based batteries at various discharge rates at 80 °C, (b) cycle-life of the DE10 based battery at various discharge rates at 25 °C.

4. CONCLUSIONS

In summary, we have presented a systematic study to understand the influence of chemical microstructure of single ion polymeric electrolyte membranes on the performance of lithium ion batteries. A series of single ion polymer electrolytes with varying ratios of aliphatic and aromatic moieties for control of porosity in the SIPE membranes formed with PVDF-HFP was synthesized. It was demonstrated that the membrane porosity increases with the aromatic content in the polymers, as confirmed by the measured solvent uptake capacities and the SEM images of the membranes. It was found that appropriate membrane porosity enhances ionic conductivity, reduces interfacial resistance between electrodes and electrolyte and ultimately boosts performance of Li-ion batteries. Despite the excellent performance of the DE10 cell at both 25 and 80 °C, it remains a question whether the size and the type of porosity present in the membrane are the optimal. Clearly, the pore size must be large enough to accommodate a sufficient amount of solvent; however, at the same time, it must also be small enough to allow the solvated Li^+ ions to be in close contact with the walls of the conduction channels to minimize concentration polarization in the membranes. Furthermore, the present study utilized only one type of aromatic component to gain understanding on the influenece of chemical microstruture on porosity and electrochemical properties. The effects of aromatic moiety selection on these properties have not been addressed and are expected to be significant. Nevertheless, the results presented in the present study provide important physical insight into the relationship between the microstructures of SIPE membranes and battery performance.

AUTHOR INFORMATION

Corresponding Authors

*E-mail: chghs2@gmail.com. Tel: 86-27-678833049. Fax: 86-27-67883808.

*E-mail: sunyubao@gmail.com

Notes

The authors declare no competing financial interest.

ACKNOWLEDGMENTS

The authors gratefully acknowledge support of a Start-up grant from NUS, a POC grant from National Research Foundation of Singapore, Singapore−Peking−Oxford Research Enterprise (SPORE), and the National Natural Science Foundation of China (21233006).

REFERENCES

(1) Scrosati, B.; Garche, J. Lithium batteries: Status, Prospects and Future. *J. Power Sources* **2010**, *195*, 2419−2430.

(2) Tarascon, J. M.; Armand, M. Issues and Challenges Facing Rechargeable Lithium Batteries. *Nature* **2001**, *414*, 359−367.

(3) Cheng, F.; Liang, J.; Tao, Z.; Chen, J. Functional Materials for Rechargeable Batteries. *Adv. Mater.* **2011**, *23*, 1695−1715.

(4) Armand, M.; Tarascon, J. M. Building Better Batteries. *Nature* **2008**, *451*, 652−657.

(5) Goodenough, J. B.; Kim, Y. Challenges for Rechargeable Li Batteries. *Chem. Mater.* **2009**, *22*, 587−603.

(6) Yamada, Y.; Furukawa, K.; Sodeyama, K.; Kikuchi, K.; Yaegashi, M.; Tateyama, Y.; Yamada, A. Unusual Stability of Acetonitrile-Based Superconcentrated Electrolytes for Fast-Charging Lithium-Ion Batteries. *J. Am. Chem. Soc.* **2014**, *136*, 5039−5046.

(7) Meziane, R.; Bonnet, J.-P.; Courty, M.; Djellab, K.; Armand, M. Single-ion Polymer Electrolytes Based on a Delocalized Polyanion for Lithium Batteries. *Electrochim. Acta* **2011**, *57*, 14−19.

(8) Feng, S. W.; Shi, D. Y.; Liu, F.; Zheng, L. P.; Nie, J.; Feng, W. F.; Huang, X. J.; Armand, M.; Zhou, Z. B. Single Lithium-ion Conducting Polymer Electrolytes Based on Poly (4-styrenesulfonyl)-(trifluoromethanesulfonyl)imide Anions. *Electrochim. Acta* **2013**, *93*, 254−263.

(9) Zhu, Y. S.; Wang, X. J.; Hou, Y. Y.; Gao, X. W.; Liu, L. L.; Wu, Y. P.; Shimizu, M. A New Single-ion Polymer Electrolyte Based on Polyvinyl Alcohol for Lithium Ion Batteries. *Electrochim. Acta* **2013**, *87*, 113−118.

(10) Scrosati, B.; Garche, J. Lithium Batteries: Status, Prospects and Future. *J. Power Sources* **2010**, *195*, 2419−2430.

(11) Xu, K. Nonaqueous Liquid Electrolytes for Lithium-Based Rechargeable Batteries. *Chem. Rev.* **2004**, *104*, 4303−4418.

(12) McOwen, D. W.; Seo, D. M.; Borodin, O.; Vatamanu, J.; Boyle, P. D.; Henderson, W. A. Concentrated Electrolytes: Decrypting Electrolyte Properties and Reassessing Al Corrosion Mechanisms. *Energy Environ. Sci.* **2014**, *7*, 416−426.

(13) Zhang, Y.; Lim, C.; Cai, W.; Rupesh, R.; Xu, G.; Sun, Y.; Cheng, H. Design and Synthesis of a Single Ion Conducting Block Copolymer Electrolyte with Multifunctionality for Lithium Ion Batteries. *RSC Adv.* DOI: 10.1039/C4RA08709G.

(14) Zhang, Y.; Sun, Y.; Xu, G.; Cai, W.; Rohan, R.; Lin, A.; Cheng, H. Lithium-ion Batteries with a Wide Temperature Range Operability Enabled by Highly Conductive sp^3 Boron-based Single Ion Polymer Electrolytes. *Energy Technology* **2014**, *2*, 643−650.

(15) Zhang, Y.; Rohan, R.; Sun, Y.; Cai, W.; Xu, G.; Lin, A.; Cheng, H. A Gel Single Ion Polymer Electrolyte Membrane for Lithium-ion Batteries with Wide-temperature Range Operability. *RSC Adv.* **2014**, *4*, 21163−21170.

(16) Frömling, T.; Kunze, M.; Schönhoff, M.; Sundermeyer, J.; Roling, B. Enhanced Lithium Transference Numbers in Ionic Liquid Electrolytes. *J. Phys. Chem. B* **2008**, *112*, 12985−12990.

(17) Cai, W.; Zhang, Y.; Li, J.; Sun, Y.; Cheng, H. Single-Ion Polymer Electrolyte Membranes Enable Lithium-Ion Batteries with a Broad Operating Temperature Range. *ChemSusChem* **2014**, *7*, 1063−1067.

(18) Krabbenhøft, K.; Krabbenhøft, J. Application of the Poisson−Nernst−Planck Equations to the Migration Test. *Cem. Concr. Res.* **2008**, *38*, 77−88.

(19) Lu, B.; Zhou, Y. C. Poisson-Nernst-Planck Equations for Simulating Biomolecular Diffusion-Reaction Processes II: Size Effects on Ionic Distributions and Diffusion-Reaction Rates. *Biophys. J.* **2011**, *100*, 2475−2485.

(20) Rohan, R.; Sun, Y.; Cai, W.; Pareek, K.; Zhang, Y.; Xu, G.; Cheng, H. Functionalized Meso/macro-porous Single Ion Polymeric Electrolyte for Applications in Lithium Ion Batteries. *J. Mater. Chem. A* **2014**, *2*, 2960−2967.

(21) Zhang, Y.; Xu, G.; Sun, Y.; Han, B.; W, T.; T, B.; Chen, Z.; Rohan, R.; Cheng, H. A Class of sp^3 Boron-based Single-ion Polymeric Electrolytes for Lithium Ion Batteries. *RSC Adv.* **2013**, *3*, 14934−14937.

(22) Bouchet, R.; Maria, S.; Meziane, R.; Aboulaich, A.; Lienafa, L.; Bonnet, J.-P.; Phan, T. N. T.; Bertin, D.; Gigmes, D.; Devaux, D.; Denoyel, R.; Armand, M. Single-ion BAB Triblock Copolymers as Highly Efficient Electrolytes for Lithium-metal Batteries. *Nat. Mater.* **2013**, *12*, 452−457.

(23) Cai, Z.; Liu, Y.; Liu, S.; Li, L.; Zhang, Y. High Performance of Lithium-ion Polymer Battery Based on Non-aqueous Lithiated Perfluorinated Sulfonic Ion-exchange Membranes. *Energy Environ. Sci.* **2012**, *5*, 5690−5693.

(24) Zorin, I. M.; Zorina, N. A.; Bilibin, A. Y. Phase Separation Two Polymers in a Blend and Selective Degradation as a Method for Porous Structure Formation. *Polym. Sci. Ser. A* **2010**, *52*, 150−159.

(25) Zhang, Y.; Ting, J.; Rohan, R.; Cai, W.; Li, J.; Xu, G.; Chen, Z.; Lin, A.; Cheng, H. Fabrication of a Proton Exchange Membrane via Blended Sulfonimide Functionalized Polyamide. *J. Mater. Sci.* **2014**, *49*, 3442−3450.

(26) Evans, J.; Vincent, C. A.; Bruce, P. G. Electrochemical Measurement of Transference Numbers in Polymer Electrolytes. *Polymer* **1987**, *28*, 2324−2328.

(27) Feng, S.; Shi, D.; Liu, F.; Zheng, L.; Nie, J.; Feng, W.; Huang, X.; Armand, M.; Zhou, Z. Single Lithium-ion Conducting Polymer Electrolytes Based on Poly[(4-styrenesulfonyl)-(trifluoromethanesulfonyl)imide] Anions. *Electrochim. Acta* **2013**, *93*, 254−263.

(28) Ghosh, A.; Wang, C.; Kofinas, P. Block Copolymer Solid Battery Electrolyte with High Li-Ion Transference Number. *J. Electrochem. Soc.* **2010**, *157*, A846−A849.

(29) Lee, K. H.; Kang, M. S.; Zhang, S.; Gu, Y.; Lodge, T. P.; Frisbie, C. D. Cut and Stick" Rubbery Ion Gels as High Capacitance Gate Dielectrics. *Adv. Mater.* **2012**, *24*, 4457−4462.

(30) Elsabee, M. Z.; Nassar, M. A.; Salah, E. M. E.-b. Preparation and Characterization of Some Aromatic/ Aliphatic Polyamides. *Am. J. Polym. Sci.* **2012**, *2*, 7−13.

(31) Watanabe, M.; Suzuki, Y.; Nishimoto, A. Single Ion Conduction in Polyether Electrolytes Alloyed with Lithium Salt of a Perfluorinated Polyimide. *Electrochim. Acta* **2000**, *45*, 1187−1192.

(32) Sun, X. G.; Kerr, J. B. Synthesis and Characterization of Network Single Iion Conductors Based on Comb-branched Polyepoxide Ethers and Lithium Bis(allylmalonato)borate. *Macromolecules* **2005**, *39*, 362−372.

(33) Tian, L.-Y.; Huang, X.-B.; Tang, X.-Z. Single-ionic Gel Polymer Electrolyte Based on Polyvinylidene Fluoride and Fluorine-Containing Ionomer. *Eur. Polym. J.* **2004**, *40*, 735−742.

(34) Wang, X.; Liu, Z.; Kong, Q.; Jiang, W.; Yao, J.; Zhang, C.; Cui, G. A Single-ion Gel Polymer Electrolyte Based on Polymeric Lithium Tartaric Acid Borate and its Superior Battery Performance. *Solid State Ion.* **1996**, *86*−*88*, 819.

(35) Jiang, J.; Gao, D.; Li, Z.; Su, G. Gel Polymer Electrolytes Prepared By in Situ Polymerization of Vinyl Monomers in Room-temperature Ionic Liquids. *React. Funct. Polym.* **2006**, *66*, 1141−1148.

(36) Voice, A. M.; Southall, J. P.; Rogers, V.; Matthews, K. H.; Davies, G. R.; McIntyre, J. E.; Ward, I. M. Thermo Reversible Gel Polymer Electrolyte. *Polymer* **1994**, *35*, 3363.

(37) Geiculescu, O. E.; Yang, J.; Zhou, S.; Shafer, G.; Xie, Y.; Albright, J.; Creager, S. E.; Pennington, W. T.; DesMarteau, D. D. Solid Polymer Electrolytes from Polyanionic Lithium Salts Based on the LiTFSI Anion Structure. *J. Electrochem. Soc.* **2004**, *151*, A1363−A1368.

(38) Zhu, Y.; Xiao, S.; Shi, Y.; Yang, Y.; Wu, Y. A Trilayer Poly(vinylidene fluoride)/polyborate/poly(vinylidene fluoride) Gel polymer Electrolyte with Good Performance for Lithium Ion Batteries. *J. Mater. Chem. A* **2013**, *1*, 7790−7797.

(39) Croce, F.; Appetecchi, G. B.; Persi, L.; Scrosati, B. Nanocomposite Polymer Electrolytes for Lithium Batteries. *Nature* **1998**, *394*, 456−458.